EBUG: Elastic-beam Buckling and Undulating Generation for Multi-modal Robot Locomotion in Environmental Exploration

Siyue Yao[1], Hao Li[5], Yuliang Lu[2], Chenhao Wu[3], Mark R. Cutkosky[5], and Genliang Chen[4,*]

***Abstract*— Multi-modal locomotion significantly enhances the mobile capabilities of robots in field environments. However, existing realizations rely on complex mechanical systems, are vulnerable to external interferences, and incur high costs. This paper proposes EBUG, a robot using elastic beams as motion generation units. Two patterns, crawling and jumping, are achieved through undulating deformations and the snap-through buckling process of a single beam. The kinetostatic and dynamic models are established based on a discretization method, facilitating analysis and rapid optimization. Under such a simple design, the total cost of EBUG is less than $5 while showcasing comprehensive motion abilities, including going straight and making turns with distinct radius. EBUG PRO ($59\,g$), with actuations of higher performance, can crawl at $28\,mm/s$, $0.4\,BL/s$ (Body Length per second), and achieve consecutive jumps, at a moving speed of $106.1\,mm/s$ ($1.5\,BL/s$). The maximum jumping height is $61\,mm$, $4.1\,BT$ (Body Thickness). Meanwhile, asymmetric motions are generated by tuning the restriction angles for both patterns, achieving turnings at $18\,°/s$. In addition, the combination and switching between crawling and jumping enhances adaptation and motion performance across various terrains and endows obstacle crossing ability.**

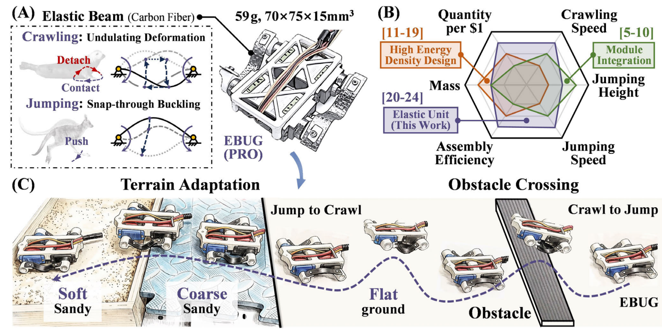

Fig. 1. Overview of EBUG. **(A)** Generation principles of crawling and jumping patterns based on one elastic beam. **(B)** Comparison with other existing designs. **(C)** Achieve terrain adaptation and obstacle crossing for applications in environmental exploration by switching between patterns.

I. INTRODUCTION

Caterpillars utilize undulation-driven crawling to traverse sand, grass, and concrete; locusts employ powerful jumping to overcome pebbles and leaf litter; crickets robustly integrate two patterns, enabling rapid and adaptive movement across wild scenarios where a single mode would be insufficient –all these creatures inspire that multi-modal locomotion enhances and broadens the functions and performance for mobile robot designs, raising competitiveness in environmental explorations [1]–[3]. However, existing implementations depend on complex systems or external stimuli [4], lacking simple yet effective, high-performance, and cost-efficient designs.

One direct method is to integrate several motion generation units that are required for multiple patterns [5]–[7]. Sihite et al. [8] combined components of wheels, thrusters, and legs, achieving eight types of motions, greatly enhancing the capacity to negotiate multi-substrate environments. Chae et al. [9] applied a clutch to adjust the jumping height. Yim et al. [10] presented a $95.7\,g$ robot, integrating tripod links for crawling and a jumping mechanism, which crawls $39.4\,mm/s$ ($0.4BL/s$) and jumps $190\,mm$ ($2.2\,BT$). However, integration of modules, as well as additional tuning mechanisms, inevitably leads to complex mechanical and control systems.

Another method is to take advantage of actuation with high energy density to achieve outstanding motion capacities with lightweight robots [11]–[13]. Singh et al. [14] devised a $0.98\,g$ robot that can easily jump $500\,mm$ ($38.5\,BT$). Wang et al. [15] adopted adjustable tensions in a $1.2\,g$ robot, achieving $1.16BL/s$ speed and $13.06\,BT$ jumping height. Lin et al. [16] constructed a g-level robot with $200\,mm/s$ ($2.0\,BL/s$) mimicking caterpillars rolling. Huang et al. [17] developed a $0.46\,g$ robot, validating $29.87\,mm/s$ ($1.2\,BL/s$) movement speed with jumping pattern. Wu et al. [18], [19] explored modular origami units to broaden the abilities of assembling and turning. Nevertheless, these design frames show a deficiency in recovery speed, consecutive motions, and a limited domain to naturally integrate distinct patterns.

Researchers have made efforts to utilize elastic units due to the intrinsic compliance, which leads to simple designs with fewer actuators. Ta [20] applied precompressed tensions to actuate a flexible beam into an S-shape, supporting undulation locomotion. Besides, the buckling phenomenon aroused interest due to its rapid response [21]. Li et al. [22] utilized two antagonistic springs to trigger the snap-through, achieving $0.56\,mm/s$ ($0.006\,BL/s$) speed and $95\,mm$ ($2.4\,BT$) height with $150\,mm$ ($1.5\,BL$) forward for one jump. Grossi et al. [23] presented buckling-driven elastomeric auxetic modules to mimic the crawling of caterpillars, achieving $5.8\,mm/s$

*This work was supported in part by the Science and Technology Commission of Shanghai Municipality under the Grant 25511104200 and the National Natural Science Foundation of China under the Grant 525B2057.

[1] Shanghai Key Laboratory of Digital Manufacture for Thin-Walled Structures, Shanghai Jiao Tong University, Shanghai 200240, China sy.yao@sjtu.edu.cn

[2] Shanghai Key Laboratory of Intelligent Robotics, Shanghai Jiao Tong University, Shanghai 200240, China yulianglu@sjtu.edu.cn

[3] META Robotics Institute, Shanghai Jiao Tong University, Shanghai 200240, China g.rotrix@sjtu.edu.cn

[4,*] State Key Laboratory of Mechanical Systems and Vibration, Shanghai Jiao Tong University, Shanghai 200240, China (Corresponding: leungchan@sjtu.edu.cn)

[5] Department of Mechanical Engineering, Stanford University, USA (li2053@stanford.edu, cutkosky@stanford.edu)

($0.05\,BL/s$). Yeh et al. [24] explored combining the undulating deformation and buckling of elastic units to achieve hopping and crawling, which moves at $5.8\,mm/s$ ($0.02\,BL/s$). To sum up, elastic units possess intrinsic deformation and energy storage-release capacities, promoting a high degree of freedom under limited actuators, thus suitable for integrating different patterns. However, the design, performance, and cost of the mobile robot remain to be improved.

To this end, the contributions of this paper include:

- Propose a framework of leveraging the deflection and energy storage properties of elastic beams, other than direct drive by actuators, to generate multi-modal motions (crawling and jumping) with better performance through undulating deformation and snap-through buckling.
- Establish the analytical kinetostatic and dynamic models for the beams to facilitate analysis and optimal design.
- Present straightforward strategies for motion adjustment (turning) by tuning the restriction angle of actuators.
- Achieve performance of $28\,mm/s$ ($0.4\,BL/s$) and $18\,°/s$ for crawling and $106.1\,mm/s$ ($1.5\,BL/s$) for jumping. The highest jump reaches $61\,mm$ ($4.1\,BT$).
- Exhibit terrain adaptation and obstacle crossing abilities, highlighting potentials in environmental exploration.

This paper is organized as follows: principles, modeling, and designs are elaborated in Sec. II. Sec. III presents the functions and performance of EBUG. Sec. IV demonstrates terrain adaptation and obstacle crossing, with discussion and future work in Sec. V. Conclusions are drawn in Sec. VI.

II. DESIGN AND MODELING

A. Crawling and Jumping Patterns

The basic design concept of EBUG leverages the deformation of an elastic beam to realize different patterns. Actuated at both ends, the beam deforms into an undulating shape, which is suitable for mimicking the crawling pattern, like a seal. As depicted in Fig. 1(A), an intermediate region of the beam moves up and down in an approximately linear trajectory under a certain pattern of the actuators. Combining the assumption that no slipping occurs for the contact region with the ground, an enclosed and cyclic motion can be generated. It should be noted that crawling is achieved only when the contact region detaches from the ground during the upward deformation of the beam; otherwise, the robot swings back and forth without moving forward. Specific parameters of the mechanism and beams are obtained based on the kinetostatic model established in Sec. II-B.

The jumping pattern is achieved by the burst of energy. As shown in Fig. 1(A), the snap-through buckling process is triggered, changing from a high-energy state to a low-energy one under the same actuation rapidly, often at $10\,ms$-level. An effective jump is generated when the contact with the ground occurs during the buckling. It should be noted that the released energy alters when the actuation is different. The height of EBUG from the ground, as well as the beam parameters and actuation angles, are devised according to the dynamic model established in Sec. II-B.

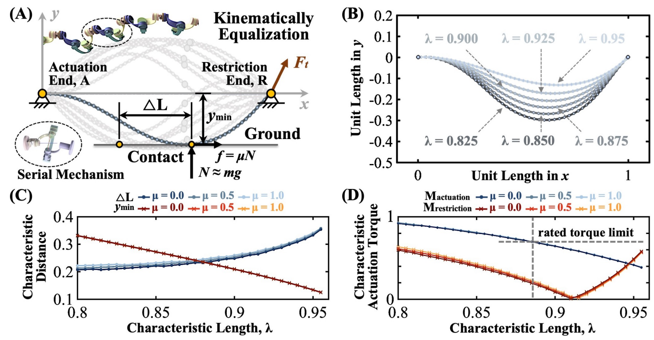

Fig. 2. Kinetostatic modeling of the elastic beam. **(A)** Geometric and force restrictions. **(B)** Deformation under different characteristic length ($\lambda = L_{AR}/L_{beam}$) with the same actuation. **(C)** Characteristic distance and **(D)** actuation torque variance relative to λ.

B. Kinetostatic and Dynamic Modeling of Elastic Beam

The large deflection problem for an elastic beam can be modeled using the discretization-based compliance decomposition method [25]. As illustrated in Fig. 2(A), the elastic beam is separated into n segments with equal length. Each segment is kinematically equalized to a serial mechanism with rigid links and elastic joints. The kinetostatic model composes geometric and force constraints into a set of nonlinear algebraic equations as We should clarify the notation in the upper equation below

$$\boldsymbol{c}\left(\boldsymbol{\Theta}, \boldsymbol{F}_t, \boldsymbol{F}_k\right) = \begin{bmatrix} \left(\log\left(\mathbf{g}_{\boldsymbol{\Theta}} \cdot \mathbf{g}_{t,\theta_r}^{-1}\right)\right)^{\vee} \\ \mathbf{K}_s \cdot \boldsymbol{\Theta} - \mathbf{J}_{t,\boldsymbol{\Theta}}^T \cdot \boldsymbol{F}_t - \mathbf{J}_{k,\boldsymbol{\Theta}}^T \cdot \boldsymbol{F}_k \end{bmatrix} = \boldsymbol{0} \quad (1)$$

where superscript Vee denotes the vector space representation of the log map of the Lie Group. $\boldsymbol{\Theta} = [\theta_1, \theta_2, ..., \theta_n]^T \in \mathbb{R}^{n\times 1}$ represents joint variables, specifically the rotational angle for planar cases. $\mathbf{g}_{\boldsymbol{\Theta}} = \mathbf{T}_{\boldsymbol{\Theta}} \cdot \mathbf{g}_{\theta_a}$. $\mathbf{T}_{\boldsymbol{\Theta}}$ is the transformation matrix. $\mathbf{g}_{\theta_a}$ and $\mathbf{g}_{t,\theta_r}$ represent the initial and target position and pose, which are determined by the actuation and restriction angles. $\mathbf{J}_{t,\boldsymbol{\Theta}}$ and $\mathbf{J}_{k,\boldsymbol{\Theta}}$ are the Jacobian matrix mapping from joint space to workspace. $\boldsymbol{F}_t \in \mathbb{R}^{6\times 1}$ and $\boldsymbol{F}_k$ are the externally exerted forces and torques expressed in wrench form. $\boldsymbol{F}_k$ is constructed by the normal force $N \approx m \cdot g$ and the friction force $f = \mu \cdot N$ under the sliding friction assumption, exerted at the lowest segment, where the contact happens. $\mathbf{K}_s = \mathrm{diag}\{k_1, k_2, .., k_n\} \in \mathbb{R}^{n\times n}$ denotes the structural stiffness matrix of the elastic joints.

Eq. (1) can be solved using the Newton-Laphson algorithm, with an analytical gradient. ΔL denotes the ideal forward distance for one stride without sliding. The beam length is optimized to maximize ΔL under the same range and within the output limitation of actuators. The characteristic length λ, defined as the joint distance over the beam length [26], is utilized for unified analysis. Deformation of beams under distinct λ is depicted in Fig. 2(B). The variance of ΔL, height of the lowest region y_{min}, and the torques for the actuation and restriction motors related to λ under different μ are provided in Fig. 2(C)-(D). The results reveal that the influence of μ is minor due to a small gravity. ΔL increases with the increase of λ, while the required torques basically

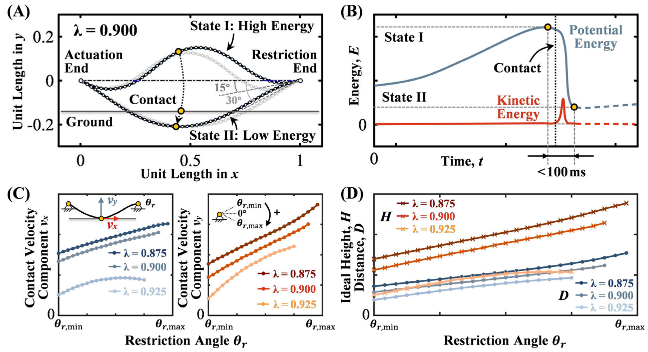

Fig. 3. Dynamic modeling of the elastic beam. **(A)** Representative snap-through buckling process. **(B)** Energy variance during buckling. **(C)** Contact velocity components and **(D)** motion variance relative to θ_r.

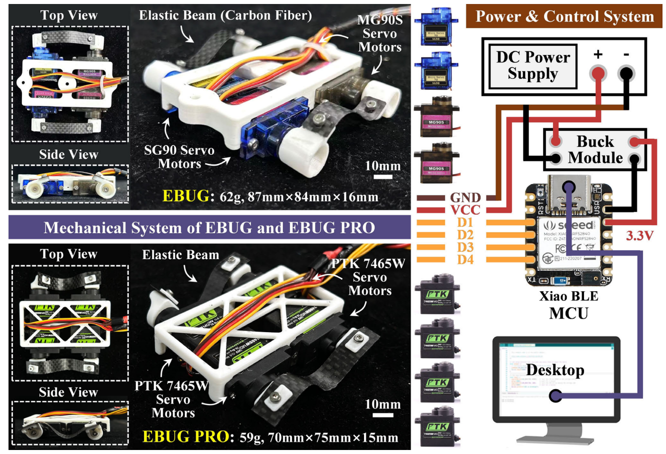

Fig. 4. Comprehensive systematic diagram of EBUG and EBUG PRO using distinct types of servo motors.

decrease. For EBUG design, a larger ΔL is desired, leading to a larger λ, which is further restricted by the torque limit. Once λ is determined, the height of EBUG should be smaller than the corresponding y_{min} to ensure contact occurrence.

Further, the snap-through buckling process is simulated by the dynamic model of the elastic beam, which can be established based on the serial mechanism equivalence as

$$\boldsymbol{\Phi} \cdot \ddot{\boldsymbol{\Theta}} + \boldsymbol{C}(\boldsymbol{\Theta}, \dot{\boldsymbol{\Theta}}) = \boldsymbol{Q} \tag{2}$$

where $\boldsymbol{\Phi}$ is the generalized inertia matrix. $\boldsymbol{C}(\boldsymbol{\Theta}, \dot{\boldsymbol{\Theta}})$ denotes the elastic terms, where the damping is neglected. $\boldsymbol{Q}$ is the generalized force. The formula is expressed in wrench form.

The energy variance during buckling is depicted in Fig. 3(B), where the potential energy decreases continuously while the kinetic energy first increases from zero and then decreases back to zero. Without considering energy loss, earlier contact leads to better jumping conditions due to higher energy conversion efficiency and a longer contact time. Therefore, the height of EBUG is set as low as possible. Once the height is determined, simulations are carried out to acquire the contact velocity variance relative to different θ_r for distinct λ. Herein, the contact velocity components are considered directly related to the contact force, which is positively correlated with the jump height and the forward distance. The results are shown in Fig. 3(C). Both velocity components increase with a reduction in λ, indicating a stronger force related to a beam with larger deflections. Besides, when θ_r increases, the vertical component v_y basically increases while the horizontal one v_x either increases or first increases and then drops for distinct λ. The fluctuations are induced by which stage and which region the contact occurs, which differs due to a different deformation with the same height. This provides a straightforward strategy for adjusting the motion by tuning θ_r and indicates a potentially controllable locomotion. Further, the jumping height H and forward distance D are calculated based on an oblique projectile motion, depicted in Fig. 3(D), where both indicators basically increase with a larger θ_r.

C. System Integration of EBUG

Based on the theoretical analysis, EBUG is constructed using four servo motors, with every two motors actuating one elastic beam at both ends. The motors are connected utilizing a carved 3D-printed PLA base, reducing the weight as much as possible. The beam is made of carbon fiber (CF) for both fine elasticity and manufacturing convenience. The rotational joints are set to a minimum height of $6\,mm$ from the ground, with a distance of $50\,mm$. The selection of λ is a balance between two patterns. Crawling demands a larger ΔL with a larger λ while jumping a larger H and D with a smaller λ. Eventually, jumping is ensured prior. $\lambda = 0.87$ is applied, considering the height and rated torque limits.

The comprehensive system is illustrated in Fig. 4. The four motors are connected to a small MCU, namely Xiao BLE, through four I/O interfaces, which are further controlled by a desktop. The power system includes a DC power supply that provides the required voltage for motors and supplies $3.3\,V$ to the MCU through an additional buck module.

EBUG utilizes two SG90 and two MG90S servo motors, which are the cheapest within a small weight, a compact size, and a large output torque ($2.0\,kg \cdot cm$ under $5\,V$ power supply). The overall weight for EBUG is $62\,g$ with a size $87\,mm \times 84\,mm \times 16\,mm$. The total manufacturing cost for one EBUG is less than $\$5$, showcasing unparalleled advantages.

Meanwhile, EBUG PRO applies servo motors, namely the PTK 7465W, with better performance. The motors are water-proof, and can provide a rated torque up to $5.8\,kg \cdot cm$ under $8.4\,V$ power supply. The overall weight for EBUG PRO is $59\,g$ with $70\,mm \times 75\,mm \times 15\,mm$ in size, reduced due to a lighter base. The cost is higher (about \$30). However, the functions and performance of the mobile robot are enhanced.

III. VALIDATION AND EVALUATION

A. Crawling Pattern Locomotion

The crawling pattern locomotion is achieved through the undulating deformation of the elastic beams. As discussed in Sec. II-A, the crawling pattern requires a non-reciprocating closure trajectory for the contact point, which is achieved by the periodical actuation at the two ends of the elastic beam with a phase difference. The utilized actuation pattern is depicted in Fig. 5(A). Through the angle variance, it

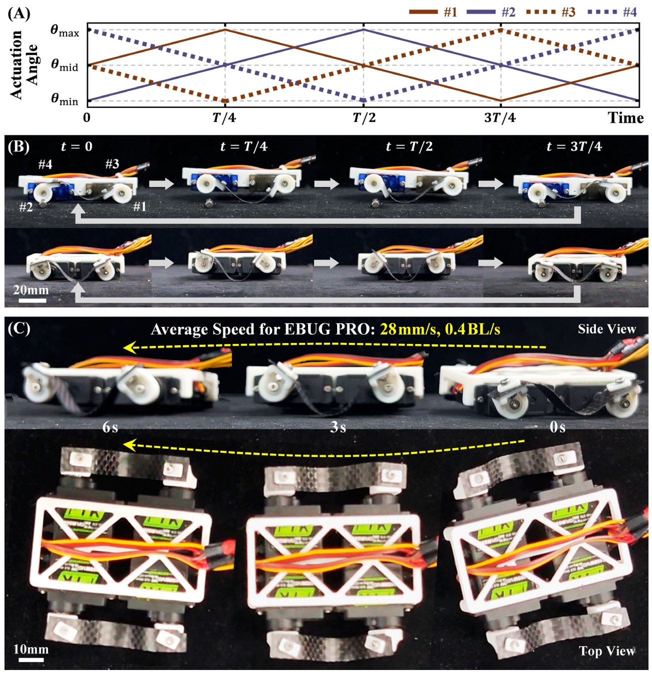

Fig. 5. Generation and evaluation of the crawling pattern locomotion. **(A)** Angle variance of the four servo motors to achieve undulating deformation of the elastic beams. **(B)** Corresponding frames within one period of crawling pattern for EBUG and EBUG PRO. **(C)** The highest locomotion speed of EBUG PRO under the crawling pattern.

can be seen that the motors closer to the rear of EBUG lead those closer to the head by $\pi/2$ phase, which is also a quarter of one period ($T/4$), for both sides. Moreover, the two sides differ from each other by an additional π phase, half of one period ($T/2$). This leads to the result that when one side is touching down on the ground, the other side is moving backward in the air. Two sides work in turn, resulting in a periodical crawling locomotion with a higher speed. The undulating deformation of beams and the crawling motion are illustrated in Fig. 5(B), where the sub-periods and numbering of the motors correspond to those in (A). From the figures, it can be seen that the deformation of the elastic beams geometrically matches the result of the proposed kinetostatic model, validating the effectiveness. In addition, a period of crawling of EBUG PRO is recorded to demonstrate its locomotion performance, as shown in Fig. 5(C). It should be noted that the rotational speed for the servo motors has been tuned to its maximum value, which is about $1\,ms/^{\circ}$. Under such circumstances, the average speed is the highest, reaching about $28\,mm/s$, which is $0.4\,BL/s$.

Distinct crawling patterns can be utilized to generate more complicated motions, including turning. The angle variance in Fig. 5(A) leads to a straight locomotion, which is achieved by the phase difference between the two motors on the same side. Therefore, a different phase lead or lag, within the same rotation range, is capable of tuning the motion directions.

Following such a perspective, the angle variances for making a right or left turn are depicted in Fig. 6(A). Compared with the angle variance in Fig. 5(A), it can be seen that when

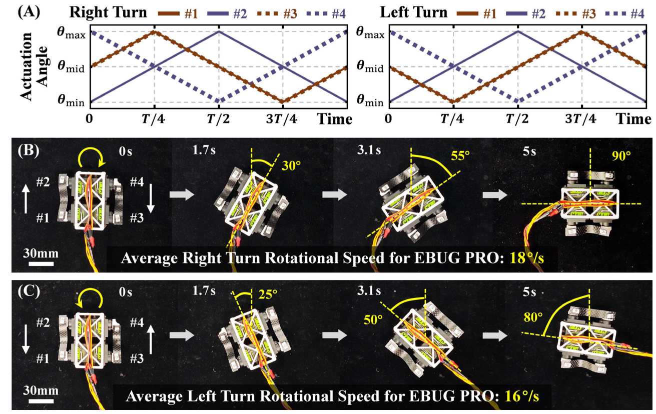

Fig. 6. Functional verification of turning based on distinct crawling patterns. **(A)** Angle variance of the four servo motors to achieve right and left turns. **(B)** Corresponding frames for EBUG PRO when turning right. **(C)** Corresponding frames for EBUG PRO when turning left.

making a right turn, the angles for servo motors #1, #2, and #4 are the same, while that for #3 changes for a π phase, half of one period ($T/2$). This leads to a result that the previously $\pi/2$ leading phase for #3 than #4 changes to a $\pi/2$ lagging phase. Further, the elastic beam actuated by motors #3 and #4 undulates in an opposite direction and eventually leads to a rotation towards the right for EBUG PRO, as illustrated in Fig. 6(B). Similarly, the angle variances for making a left turn are the same as going straight for motors #2, #3, and #4. Only the variance for motor #1 changes for half a period, resulting in a $\pi/2$ lagging phase than #2. Subsequently, EBUG PRO is able to turn left as demonstrated in Fig. 6(C). From the figures, it can be seen that the average rotational speed for turning right and left is $18^{\circ}/s$ and $16^{\circ}/s$, respectively. It should be noted that the four motors on EBUG PRO are the same, indicating that if both the angles for #1 and #3 change for half a period, it is possible to move backward.

The speed difference in turning is attributed to the inconsistency of the elastic beams on the two sides, which may be caused by a distinct length of the beam, assembly errors, a difference in motor shaft distance, and twisting of the elastic beams. This inconsistency can also be observed in Fig. 5(C), where the top view shows that EBUG PRO moves along a slightly rightward-tilted straight line, which is consistent with the result that the rotational speed for making a right turn is higher. It should be further noted that the right and left turns in the experiments are theoretically rotations relative to EBUG PRO itself. Distinct frequencies, ranges, and phase differences for the motor angle variances should be considered to achieve a more complicated motion, including rotations with a certain curvature and speed, which are further elaborated in the discussion section.

B. Jumping Pattern Locomotion

The jumping pattern is generated by leveraging the snap-through buckling process, as analyzed in Sec. II-A. The complete process of one step of jumping, which is activated by the elastic beam on one side, can be categorized into four stages, as depicted in Fig. 7(A). Firstly, the servo

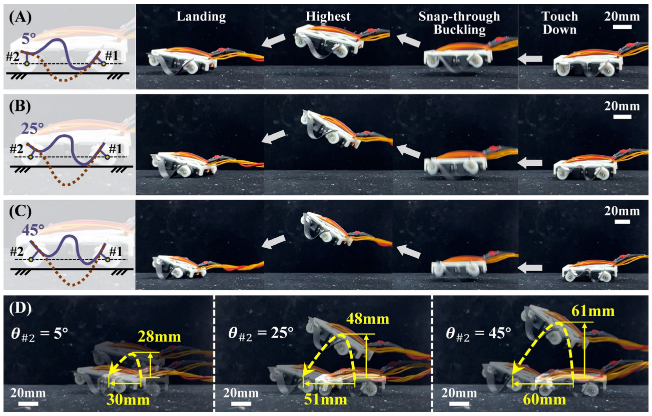

Fig. 7. Different height and forward distance of jumping by tuning the θ_r. Corresponding frames of the four stages during one step by the elastic beam on one side under restricted angle being **(A)** 5°, **(B)** 25°, and **(C)** 45°. **(D)** Integrated image of one step of jumping under different restricted angles, with the maximum height and forward distance being labeled.

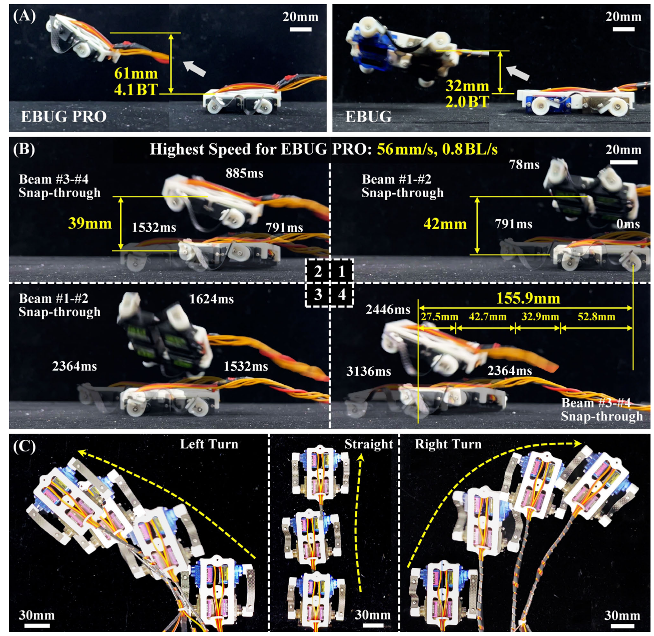

Fig. 8. Performance and function of EBUG and EBUG PRO using the jumping pattern, including height and moving speed. **(A)** The highest jumping height under a certain value of θ_r. **(B)** Frames of four consecutive snap-through buckling of the elastic beams to achieve continuous locomotion. **(C)** Achieve forward and turning motions through tuning θ_r.

motor at the restriction end, namely #2, rotates to a given angle. The motor at the actuation side, namely #1, rotates gradually until the elastic beam is close to the snap-through buckling limitation. Subsequently, motor #1 further actuates, surpassing the limitation, which leads to the occurrence of the snap-through buckling phenomenon. The elastic beam touches down on the ground and pushes EBUG PRO into the air. Furthermore, EBUG PRO reaches the highest position and then lands on the ground, ready for the next step of jumping by the elastic beam on the other side. It should be noted that although more energy will be released if the beams on both sides buckle at the same time, which can push EBUG PRO higher and farther, the slight inconsistency at both sides often prevents a simultaneous trigger and wastes energy instead. As a consequence, the beams buckle in turn, which utilizes the energy more efficiently in a periodic manner.

Different restricted angle results in distinct deformation of the elastic beam at the buckling limitation, which further influences the pushing force. As shown in Fig. 7(A)-(C), three restricted angles, including 5°, 25°, and 45°, are applied to initialize the deformation of the elastic beam before buckling. Herein, 0° is defined as the horizontal pose with the downward direction as the positive value. The two states with different stored energy at the snap-through buckling limitation are depicted in the figures, indicating that the deformation and energy release under distinct θ_r alter accordingly. Detailed analysis is provided in Sec. II-B. For the experimental cases, $\theta_r = 45°$ corresponds to a larger energy release in both horizontal and vertical directions than 25°, while 5° corresponds to the smallest ones, which align with the modeling results. The frames of EBUG PRO status under the three cases are demonstrated in the figures, and a comprehensive comparison is shown in Fig. 7(D), where the three stages of touching down, jumping to the highest position, and landing are depicted in one figure. From the results, it can be seen that the height of one step of jumping increases from 28 mm for 5°, to 48 mm for 25°, and eventually 61 mm for 45°. Meanwhile, the moving distance increases from 30 mm for 5°, to 51 mm for 25°, and eventually 60 mm for 45°. It should be noted that PTK motors have not reached the torque limitation. However, the corresponding pushing force is sufficient, as a larger one may lead to rollover since the beams are arranged on the sides.

The performance of EBUG and EBUG PRO, including the jumping height and the moving speed, is tested. As demonstrated in Fig. 8(A), the highest stable jump for EBUG PRO is 61 mm, which is 4.1 BT. This is achieved by restricting the motor angle to 45°. The servo motors for EBUG possess inferior performance, both in responding speed and output torque, and thus lead to a lower height of jump and a smaller forward distance of locomotion. By tuning θ_r within the torque limitation of the motors, the highest jumping height is 32 mm, which is 2.0 BT. Moreover, the continuous buckling of the elastic beams on both sides in turn is applied to achieve robotic locomotion. The moving speed is not only related to the forward distance of one step of jumping, but is influenced by the actuation and recovery time of the motors as well. Through experiments, the highest moving speed is obtained when $\theta_r = 20°$. Frames of four consecutive jumps are illustrated in Fig. 8(B). For the jump due to the snap-through buckling of the elastic beam at the side of motors #1 and #2, the jumping height is about 42 mm, while that for the jump caused by the other side is about 39 mm. This result is consistent with that in Fig. 7. The average time from touching down to the highest position in the air is about 90 ms. However, it takes more time, about 800 ms for one jump, considering the landing process and the recovery time for EBUG PRO and the motors. For the four jumps, the forward distances are $52.8\,mm$, $32.9\,mm$, $42.7\,mm$, and $27.5\,mm$, respectively. It can be seen that the jumping distance for the beam on the side of #1 and #2 is larger than that for the other side, which is also attributed to the inconsistency of the two sides. Two jumps form a complete cycle. EBUG PRO moves $85.7\,mm$ forward during the first cycle and $70.2\,mm$ during the second cycle. This is in part influenced by the inconsistency and in part by the effect of the tethers, which is further elaborated in the discussion section. For the first cycle, the locomotion speed can be deduced as $56\,mm/s$, which is $0.8\,BL/s$. Compared with the crawling pattern, the jumping pattern showcases its advantage in a larger moving speed, nearly two times.

Furthermore, leveraging the relationship between the contact force and θ_r, more complicated motions can be achieved, including making left and right turns, as shown in Fig. 8(C). The controlling strategy is that the elastic beam corresponding to the outer side of the turning provides a larger contact force in the forward direction than that to the inner side. Specifically, motors on both sides are given $\theta_r = 20^\circ$ when EBUG goes straight. The moving speed can be deduced as $39.4\,mm/s$, which is $0.45\,BL/s$, slower than EBUG PRO due to an inferior performance of motors. When making a left turn, the motor on the right side of EBUG provides $\theta_r = 30^\circ$ while that on the left side provides 10°. This makes the buckling of the beam on the right side more powerful, leading to a left turn after several cycles of jumping. Similarly, the motor on the left side is constrained at 10° while that on the right side is at 30° when making a right turn.

IV. DEMONSTRATIVE EXPERIMENTS

A. Adaptation to Various Terrains

Utilizing the elastic beam to achieve the multi-modal locomotion of crawling and jumping patterns is beneficial for enhancing the adaptation and performance to various terrains. The jumping pattern typically shows a higher locomotion speed than the crawling pattern. As demonstrated in Fig. 9(A), both patterns can achieve locomotion on the smooth ground. However, the crawling speed is $20.9\,mm/s$, which is $0.3\,BL/s$, slower than the speed of moving on the fabric ground as shown in Fig. 5(C). On the contrary, the jumping speed is five times faster than crawling, reaching $106.1\,mm/s$, which is $1.5\,BL/s$, faster than jumping on the fabric ground. This is because the smooth ground provides less friction than the fabric ground. The crawling pattern depends on the friction to move forward, while the jumping pattern relies on the energy release. As a consequence, less friction leads to a slower speed of crawling, yet consumes less energy during the snap-through buckling process of jumping. More energy is transformed into EBUG PRO, resulting in a higher speed. It should be noted that EBUG PRO moves more stably when crawling than jumping, though with a slower speed.

Despite outstanding performance, the jumping pattern loses efficacy on loose terrains, such as sandy ground. Frames of two steps of jumping on the sand are demonstrated in Fig. 9(B), where the snap-through buckling transmits the energy into the kinetic energy of the gravel, leading to

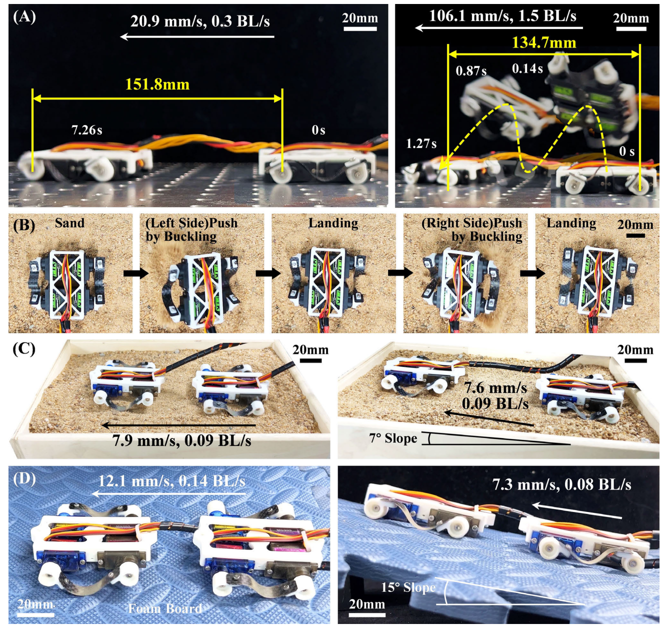

Fig. 9. Adaptation to various terrains based on multi-modal locomotion of crawling and jumping patterns. **(A)** Jumping on the smooth ground moves five times faster than crawling. **(B)** Jumping pattern can not achieve movement on the sand. **(C)** Crawling pattern can generate stable locomotion on the sand, both flat and with a slope. **(D)** Crawling pattern can generate stable locomotion on the foam board, both flat and with a slope.

only vertical jumps of EBUG. In comparison, the crawling pattern can achieve locomotion on the sand, as illustrated in Fig. 9(C). The moving speed is relatively slower, which is $7.9\,mm/s$. Moreover, EBUG maintains the locomotion capacity when the sandy ground has an inclination degree, where 7° is tested. The moving speed is $7.6\,mm/s$. It can be seen that the speed is slightly reduced due to the inclination. In addition, the crawling pattern can also generate locomotion on coarse and soft terrains. As depicted in Fig. 9(D), EBUG moves at an average speed of $12.1\,mm/s$ on a flat foam board, while at $7.3\,mm/s$ when the foam board has a 15° slope. The speed reduction is greatly influenced by the inclination.

B. Obstacle Crossing Capacity

The complementary enhancement of locomotion capacity by crawling and jumping patterns is not only reflected in adaptation to various terrains, but in reinforced motion ability as well. The jumping pattern facilitates the crossing of obstacles that cannot be climbed using the crawling pattern. As illustrated in Fig. 10(A), a narrow obstacle with the size of $5\,mm \times 5\,mm$, which is $0.07\,BL \times 0.33\,BT$, is placed in front of EBUG PRO. One step of jumping is enough to cross over the obstacle by utilizing the kinetic energy during the landing process. For a wider obstacle, as depicted in Fig. 10(B), two steps of jumping are required. The obstacle is of the size $35\,mm \times 7\,mm$, which is $0.5\,BL \times 0.5\,BT$. The height of the obstacles determines whether EBUG PRO can jump over or not, since one jump is able to take it onto the upper surface of the obstacle. Although EBUG PRO is capable of jumping to the height of $4.1\,BT$, the forward distance is critical to decide

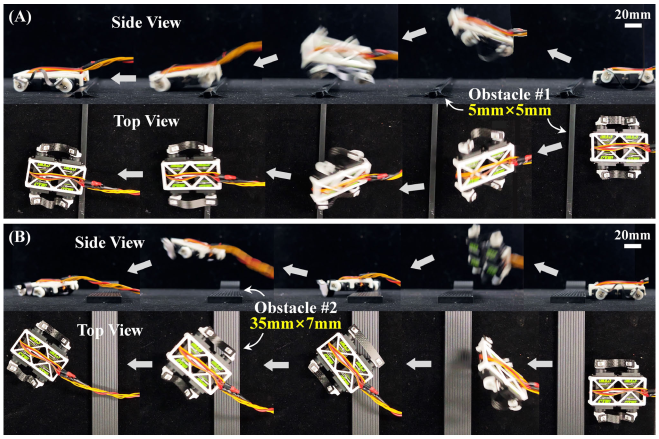

Fig. 10. Obstacle crossing based on the jumping pattern. **(A)** Cross a narrow obstacle ($0.07BL \times 0.33BT$) through one step of jumping. **(B)** Cross a wide obstacle ($0.5BL \times 0.5BT$) through two steps of jumping.

a successful crossing. This is because the contact region for the jumping pattern is relatively narrow, and thus, the place that EBUG PRO lands greatly influences whether the next jump is effective. Subsequently, the obstacle must be crossed within one jump, or it cannot be crossed. Through tests, the maximum height of the obstacles that EBUG PRO can cross over at a high success rate is $0.5BT$. The initial pose before the first jump is significant. The closer EBUG PRO is to the obstacle, the more likely it is to cross over.

C. Comprehensive Demonstration

Comprehensive demonstrations of the locomotion under distinct terrains and the complete obstacle crossing are tested. As shown in Fig. 11(A), EBUG is crossing complex terrains, including a fabric ground, a foam board, and a sandy ground. For speed performance, the jumping pattern is utilized on the fabric ground. Subsequently, EBUG switches to the crawling pattern to overcome the foam board with a slope in a more stable manner, although the jumping pattern is still effective. Eventually, the crawling pattern is maintained when entering the sandy ground since the jumping pattern loses efficacy. Therefore, the flexible switching between the two modes enhances the environmental adaptation and motion capacity.

Besides, the complete obstacle crossing process is displayed in Fig. 11(B)-(C), where multi-modal motions are applied. As discussed in Sec. IV-B, the pose before the first jump should be close to the obstacle, which is achieved through crawling. Specifically, EBUG PRO first approaches the obstacle by crawling until it bumps. Subsequently, it switches to the jumping pattern, using several consecutive jumps to cross the obstacle. Afterwards, it switches back to crawling, moving forward in a more stable mode. As a consequence, the integration and switching of the two modes broaden the capacity and applications of the mobile robot.

V. Discussion and Future Work

Motion capacities and performance, as well as terrain adaptation and obstacle crossing abilities, are verified. However, there are limitations and space for improvement.

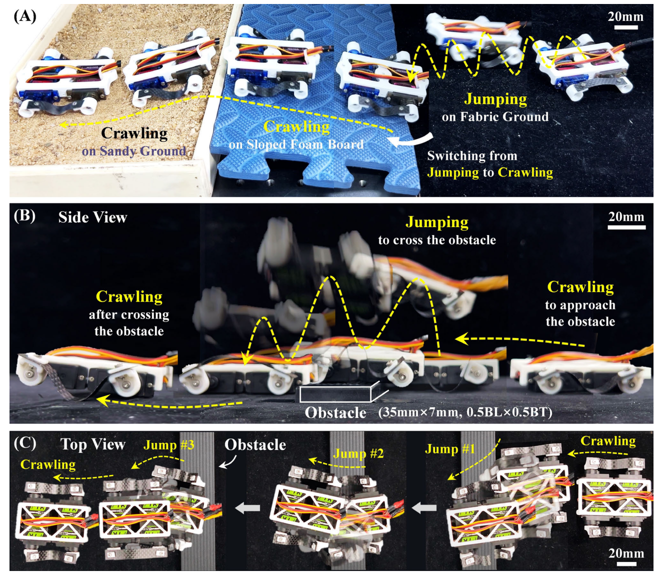

Fig. 11. Comprehensive applications of utilizing two patterns. **(A)** Jump for a higher speed and crawl to overcome distinct terrains. **(B)** Side view and **(C)** top view frames of a complete obstacle crossing, including approaching by crawling, crossing over by jumping, and leaving by crawling.

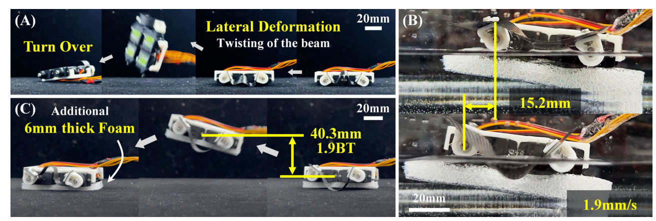

Fig. 12. Potential future work. **(A)** Twisting of the elastic beam provides lateral contact forces. **(B)** Locomotion demonstration on the water surface. **(C)** Jumping pattern for EBUG PRO with a larger thickness.

1. Inconsistency between the two sides: Due to manufacturing and assembly errors, real-time control performance, and motion inaccuracy of motors, inconsistency inevitably exists for EBUG. This manifests slightly for crawling, yet affects greatly for jumping, as simultaneous buckling cannot be guaranteed. However, environments may lead to differences between the two sides, even if these factors are overcome. Therefore, buckling in turn is reasonable and necessary.

2. Controlling strategy for complicated motions: The applied motor controlling strategies are simple yet sufficient to demonstrate the capacity of moving and turning. However, the contact situations and forces can be adjusted by tuning θ_r and θ_a for jumping. Besides, the motion curve, frequency, range, and phase differences of motors can be devised to adjust the motions when crawling. This indicates the potential for achieving more controllable motions, including turning at a given speed and curvature. Moreover, the elastic beam possesses a high degree of compliance. As demonstrated in Fig. 12(A), the twisting of the beam may bring lateral forces. Therefore, there is a probability to achieve lateral motions.

3. Exploring motions in different environments: The undulating deformation leads to a wavy pattern for achieving crawling. This is beneficial for other environments, like on the water surface [27]. Preliminary tests are carried out to illustrate the amphibious potential of EBUG PRO, as depicted in Fig. 12(B), although the moving speed is relatively slow ($1.9\,mm/s$). It should be noted that the beams are wider, and a large foam board is attached, which increases the thickness and affects the patterns. Fig. 12(C) reveals a reduced jumping height due to a larger thickness. Further investigations are required to design the robot, where the proposed modeling methods are effective and beneficial. Besides, batteries can be utilized as the power supply to construct an untethered mobile robot, demonstrating potential in field applications.

4. Capacity and performance enhancement: The utilized elastic beam is simply a pure CF beam, which provides small friction forces when contacting the ground. Microstructures, like spines, can be attached to the beam surface for adhesion and anisotropic friction forces, which may be beneficial to locomotion [28]–[30]. Moreover, several EBUGs may be connected in serial to obtain a longer undulated curve, facilitating crawling in distinct terrains.

VI. CONCLUSION

In this paper, motor-driven elastic beams are utilized as motion generation units for robot design (EBUG). By leveraging the undulating deformation and buckling phenomenon, multi-modal locomotion patterns, crawling and jumping, are realized. Kinetostatic and dynamic models are proposed for analysis and optimal design. Fundamental motions, going straight and making turns, are achieved for both patterns by tuning the actuation. EBUG (PRO) can move at $28\,mm/s$ ($0.4\,BL/s$) while crawling and $106.1\,mm/s$ ($1.5\,BL/s$) while jumping. The maximum jumping height is $61\,mm$ ($4.1\,BT$). The switching of patterns enhances terrain adaptation and motion capacity, enabling obstacle crossing. The presented framework sheds light on mobile robotic designs for multi-modal locomotion, facilitating environmental exploration.

REFERENCES

[1] W. Hu, G. Lum, M. Mastrangeli, and M. Sitti, "Small-scale soft-bodied robot with multimodal locomotion," *Nature*, vol. 554, pp. 81–85, 2018.

[2] Z. Zhakypov, K. Mori, K. Hosoda, and J. Paik, "Designing minimal and scalable insect-inspired multi-locomotion millirobots," *Nature*, vol. 571, pp. 381–386, 2019.

[3] S. Panda, S. Hajra, P. Rajaitha, and H. Kim, "Stimuli-responsive polymer-based bioinspired soft robots," *Micro and Nano Systems Letters*, vol. 11, p. 2, 2023.

[4] C. Ahn, X. Liang, and S. Cai, "Bioinspired design of light-powered crawling, squeezing, and jumping untethered soft robot," *Advanced Materials Technologies*, vol. 4, no. 7, p. 1900185, 2019.

[5] B. Liu, Y. Ren, Z. Wang, S. Jin, and W. Ge, "The multimodal bionic robot integrating kangaroo-like jumping and tortoise-like crawling," *Journal of Bionic Engineering*, vol. 22, p. 1637–1654, 2025.

[6] G. Jung, C. Casarez, S. Jung, R. Fearing, and K. Cho, "An integrated jumping-crawling robot using height-adjustable jumping module," in *2016 IEEE International Conference on Robotics and Automation (ICRA)*, Stockholm, Sweden, 2016, pp. 4680–4685.

[7] G. Jung, C. Casarez, J. Lee, S. Baek, S. Yim, S. Chae, R. Fearing, and K. Cho, "Jumproach: a trajectory-adjustable integrated jumping–crawling robot," *IEEE/ASME Transactions on Mechatronics*, vol. 24, pp. 947–958, 2019.

[8] E. Sihite, A. Kalantari, R. Nemovi, A. Ramezani, and M. Gharib, "Multi-modal mobility morphobot (m4) with appendage repurposing for locomotion plasticity enhancement," *Nature Communications*, vol. 14, p. 3323, 2023.

[9] S. Chae, S. Baek, J. Lee, and K. Cho, "Agile and energy-efficient jumping–crawling robot through rapid transition of locomotion and enhanced jumping height adjustment," *IEEE/ASME Transactions on Mechatronics*, vol. 27, pp. 5890–5901, 2022.

[10] S. Yim, S. Baek, P. Lee, S. Chae, J. Lee, S. Huh, G. Jung, and K. Cho, "Development of the sub-10 cm, sub-100 g jumping–crawling robot," *Intelligent Service Robotics*, vol. 7, p. 19–32, 2024.

[11] S. Chen, Y. Cao, M. Sarparast, H. Yuan, L. Dong, X. Tan, and C. Cao, "Soft crawling robots: design, actuation, and locomotion," *Advanced Materials Technologies*, vol. 5, p. 1900837, 2020.

[12] D. Yao, I. Kim, S. Yin, and W. Gao, "Multimodal soft robotic actuation and locomotion," *Advanced Materials*, vol. 36, p. 2308829, 2024.

[13] R. Yun, Z. Liu, J. Leng, J. huang, X. Yan, and M. Qi, "A millimeter-scale multilocomotion microrobot capable of controlled crawling and jumping," *Soft Robotics*, vol. 11, pp. 361–370, 2024.

[14] S. Singh, Z. Temel, and R. Pierre, "Multi-modal jumping and crawling in an autonomous, springtail-inspired microrobot," in *2024 IEEE International Conference on Robotics and Automation (ICRA)*, Yokohama, Japan, 2024, pp. 5999–6005.

[15] X. Wang, S. Li, J. Chang, J. Liu, D. Axinte, and X. Dong, "Multimodal locomotion ultra-thin soft robots for exploration of narrow spaces," *Nature Communications*, vol. 15, p. 6296, 2024.

[16] H. Lin, G. Leisk, and B. Trimmer, "Goqbot: a caterpillar-inspired soft-bodied rolling robot," *Bioinspiration & Biomimetics*, vol. 6, p. 026007, 2011.

[17] W. Huang, W. Shang, Y. Huang, H. Long, and X. Wu, "Insect-scale smaw-based soft robot with crawling, jumping, and loading locomotion," *IEEE Robotics and Automation Letters*, vol. 7, pp. 9287–9293, 2022.

[18] S. Wu, Y. Hong, Y. Zhao, J. Yin, and Y. Zhu, "Caterpillar-inspired soft crawling robot with distributed programmable thermal actuation," *Science Advances*, vol. 9, p. eadf8014, 2023.

[19] S. Wu, T. Zhao, Y. Zhu, and G. Paulino, "Modular multi-degree-of-freedom soft origami robots with reprogrammable electrothermal actuation," *Proceedings of the National Academy of Sciences*, vol. 121, no. 20, p. e2322625121, 2024.

[20] T. Ta, "Single actuator undulation soft-bodied robots using a pre-compressed variable thickness flexible beam," in *2024 IEEE/RSJ International Conference on Intelligent Robots and Systems (IROS)*, Abu Dhabi, United Arab Emirates, 2024, pp. 1–7.

[21] S. Nishikawa, Y. Arai, R. Niiyama, and Y. Kuniyoshi, "Coordinated use of structure-integrated bistable actuation modules for agile locomotion," *IEEE Robotics and Automation Letters*, vol. 3, pp. 1018–1024, 2018.

[22] D. Li, D. Niu, G. Ye, B. Lei, J. Han, W. Jiang, F. Luo, J. Chen, H. Liu, and B. Lu, "Crawling–jumping synergic bioinspired robots harnessing electroactive bistable actuators by adjusting mechanical responses and forces," *Applied Materials Today*, vol. 24, p. 101091, 2021.

[23] B. Grossi, H. Palza, J. Zagal, C. Falcón, and G. During, "Metarpillar: Soft robotic locomotion based on buckling-driven elastomeric metamaterials," *Materials & Design*, vol. 212, p. 110285, 2021.

[24] C. Yeh, C. Chen, and J. Juang, "Soft hopping and crawling robot for in-pipe traveling," *Extreme Mechanics Letters*, vol. 39, p. 100854, 2020.

[25] G. Chen, Z. Zhang, and H. Wang, "A general approach to the large deflection problems of spatial flexible rods using principal axes decomposition of compliance matrices," *Journal of Mechanisms and Robotics*, vol. 10, no. 3, p. 031012, 2018.

[26] G. Chen, Y. Long, S. Yao, S. Tang, J. Luo, H. Wang, Z. Zhuang, and H. Jiang, "A non-electrical pneumatic hybrid oscillator for high-frequency multimodal robotic locomotion," *Nature Communications*, vol. 16, p. 1449, 2025.

[27] L. Zhu, P. Yang, F. Li, K. Wang, L. Shui, and X. Chen, "On the snake-like lateral un-dulatory locomotion in terrestrial, aquatic and sand environments," *Journal of the Mechanics and Physics of Solids*, vol. 157, p. 104629, 2021.

[28] S. Kim, M. Spenko, S. Trujillo, B. Heyneman, D. Santos, and M. Cutkosky, "Smooth vertical surface climbing with directional adhesion," *IEEE Transactions on Robotics*, vol. 24, pp. 65–74, 2008.

[29] K. Autumn, A. Dittmore, D. Santos, M. Spenko, and M. Cutkosky, "Frictional adhesion: a new angle on gecko attachment," *Journal of Experimental Biology*, vol. 209, no. 18, p. 3569–3579, 2006.

[30] A. Rafsanjani, Y. Zhang, B. Liu, S. Rubinstein, and K. Bertoldi, "Kirigami skins make a simple soft actuator crawl," *Science Robotics*, vol. 3, p. eaar7555, 2018.